



## Full Length Article

# Fabrication of bio-inspired non-fluorinated superhydrophobic surfaces with anti-icing property and its wettability transformation analysis

Xinlin Li<sup>a</sup>, Guoyong Wang<sup>b</sup>, Ana Sofia Moita<sup>c</sup>, Chengchun Zhang<sup>a</sup>, Shunhao Wang<sup>d</sup>, Yan Liu<sup>a,\*</sup>

<sup>a</sup> Key Laboratory of Bionic Engineering (Ministry of Education), Jilin University, Changchun 130022, China

<sup>b</sup> College of Materials Science and Engineering, Key Lab of Automobile Materials, Jilin University, Changchun 130025, China

<sup>c</sup> IN + - Center for Innovation, Technology and Policy Research, Instituto Superior Técnico, Universidade de Lisboa, Av. Rovisco Pais, 1049-001 Lisboa, Portugal

<sup>d</sup> Shenyang Jinyan New Material Preparation Technology Co. Ltd, Liaoning Province, China

## ARTICLE INFO

## Keywords:

Anti-icing  
Superhydrophobic  
Aluminum alloy  
Specific surface area  
Heat transfer

## ABSTRACT

Ice accumulation leads to several inconvenient and even threatening situations in cold regions. This paper reports an efficient, non-toxic and low-cost method to fabricate hierarchical superhydrophobic surfaces on aluminum alloy with a water contact angle of 155° and a sliding angle of 5°. Tests were performed in an in-house apparatus to evaluate the ice adhesion strength and ice shear strength of the as-prepared surfaces and untreated aluminum surfaces. Results show that ice adhesion strength on different wettability surfaces strongly depends on the efficient specific surface area of the ice-solid interface. The ice shear strength was determined by different ice-solid interface contact shapes. Besides, the freezing delay time was recorded and different mechanisms of the icing process were analyzed by a specific simplified heat transfer model. The de-icing and self-cleaning test shows that the air cushion on the superhydrophobic surface can prevent the melted water from secondary icing and potential contaminations, especially at low temperature. Our results indicate that the as-prepared and recovered superhydrophobic surfaces present excellent anti-/de-icing properties and the special contact conditions and heat transfer process of the ice-substrate interface contribute to the anti-icing property of the superhydrophobic surface.

## 1. Introduction

Ice accumulation on aircraft [1], wind turbines [2] and power cables [3] causes many threatening problems or even disasters. For instance, the ice accumulation on the windward surface of aircraft will directly alter the aerodynamic force. Thus, significant efforts have been made towards the development of deicing surfaces [4,5]. Superhydrophobic surfaces in nature, such as lotus leaves [6], rose petals [7], legs of water striders [8] and butterfly wings [9], show great potential in preventing ice accumulation [10,11] and arouse tremendous interest from both industry and academic research [12,13] due to their fascinating water repellency and self-cleaning properties [14,15]. Generally, ice accumulation starts from water absorbing and condensing, so surface wettability plays a paramount role in preventing ice accumulation [16]. Chemical composition and surface roughness have been proved to be the two dominant factors governing the wettability of superhydrophobic surfaces [17,18]. Therefore, many useful methods have been introduced to fabricate superhydrophobic surfaces such as the template method [19], electro-spinning [20], sol-gel method [21],

layer-by-layer technique [22], etching treatment [23,24], chemical vapor deposition (CVD) [25], electrodes galvanic deposition [26] and electrochemical deposition [27]. As numerous icephobic surfaces are reported to be developed, in the open literature, two prospects must be put forward for the evaluation of their icephobicity, namely their “anti-icing” and “deicing” properties. For the anti-icing property, Tourkine et al. [28] observed a significant delay in freezing on a superhydrophobic surface and argued that the trapped-air layer between the water droplet and the surface acted as a thermally insulating layer. Zou et al. [29] showed that a superhydrophobic surface reduced the coverage of glaze ice more efficiently than a bare (aluminum) surface, due to its ability to repel water at low temperatures. Davis et al. [30] discussed the effects of surface roughness, quantified in terms of its skewness and kurtosis, to the ice removing process by measuring the pressure necessary to remove the ice attached to aluminum surfaces. They found that all superhydrophobic surfaces could lower the ice adhesion more efficiently than a polished one, especially the surfaces with high kurtosis and shorter autocorrelation length. Besides, Wang et al. [13] proved that superhydrophobic surfaces formed with multi-

\* Corresponding author.

E-mail address: [lyyw@jlu.edu.cn](mailto:lyyw@jlu.edu.cn) (Y. Liu).

<https://doi.org/10.1016/j.apsusc.2019.144386>

Received 16 April 2019; Received in revised form 10 October 2019; Accepted 12 October 2019

Available online 25 October 2019

0169-4332/ © 2019 Elsevier B.V. All rights reserved.

scale nanoparticles could minimize the ice adhesion due the formation of air pockets between the ice and the resultant surface and due to the lubrication of overcooled water in the surface asperities. For the deicing property, Jiang et al. [31] successfully fabricated superhydrophobic SiC/CNTs coatings on thylene vinyl acetate (EVA). The temperature of these surfaces could be rapidly increased upon near-infrared light (808 nm) irradiation, achieving a highly efficient remote deicing effect. Zhao et al. [32] developed a novel multi-layered coating by the combination of the fronted electric heating coating and top super-hydrophobic coating, which possessed high-efficient electric heating and deicing performances. Despite the encouraging results reported in the studies revised here, the development of superhydrophobic surfaces with efficient anti-icing and de-icing capabilities has not yet been satisfactorily achieved. The main obstacles remain associated with an incomplete description and understanding of the heat transfer and ice adhesion mechanisms. On the other hand, several applications require that the as-prepared superhydrophobic surfaces can recover their water repellency capabilities if the surface coatings are destroyed, i.e. a self-healing ability is required to recover from extreme (superhydrophilic) regimes.

In this context, the present paper addresses an efficient, nontoxic and low-cost method for fabricating superhydrophobic surfaces. The as-prepared superhydrophobic surfaces are produced by the combination of laser-fabrication and chemical etching processes, followed with chemical vapor deposition of PDMS. The anti-icing and deicing properties of the as-prepared surfaces and untreated aluminum surface were tested. Three different models were developed to analyze the mechanisms of ice adhesion and ice shear for surfaces with different wettability. In addition, a heat transfer model was introduced to analyze the energy loss process. After heated at high temperature, the as-prepared superhydrophobic surfaces exhibited superhydrophilic characteristics due to the destruction of the PDMS coating. However, the wettability of as-prepared surfaces could be reversed from superhydrophilicity to superhydrophobicity by slow oxidization after exposure in the air for 150 days. The results, discussed in the following sections further show that these superhydrophobic surfaces are potential “ice-phobic” materials due to their unique solid-liquid-air interface, which is useful for constructing multifunctional outdoor devices.

## 2. Experimental

### 2.1. Materials

7075 Al alloy sheets (0.4 wt% Si, 0.5 wt% Fe, 2.0 wt% Cu, 0.3 wt% Mn, 2.9 wt% Mg, 0.28 wt% Cr, 6.1 wt% Zn, 0.2 wt% Ti, with the balance being Al) with the size of 20 mm × 20 mm × 1 mm, emery paper No. 400, No. 800 and No. 1500, acetone, ethanol, Copper dichloride dihydrate ( $\text{CuCl}_2 \cdot 2\text{H}_2\text{O}$ , 99.0%), polydimethylsiloxane (PDMS) were used for the experiments reported in the present study.

### 2.2. Sample preparation

7075 Al alloy sheets were polished with 500#, 800# and 1500# emery papers in turn, and cleaned with acetone, ethanol and deionized water in an ultrasonic bath for 10 min and then dried in air. Firstly, all the samples were irradiated by laser twice, to create a micro cylindrical array structure. This array is composed by micro-cavities with a diameter of 50  $\mu\text{m}$ . The distance between the centers of the microcavities is 100  $\mu\text{m}$ . The parameters tuned for laser processing are 50 W average power, 20 kHz repetition rate, 200 ns pulse duration and 500 mm/s scanning speed. Afterward, the samples were cleaned with acetone, ethanol and deionized water in an ultrasonic bath for 15 min and dried in air. Secondly,  $\text{CuCl}_2 \cdot 2\text{H}_2\text{O}$  was solved into 50 mL of deionized water (concentration of 0.05 mol/L) and was constantly stirred and submitted to an ultrasonic bath. Then the as-prepared samples were immersed into a copper chloride solution for 15 s. Afterward, all the samples, which

were labeled as Surf 1 to Surf 5, respectively, were placed in a sealed beaker with a PDMS solution and heated at 60 °C, 100 °C, 140 °C, 180 °C and 220 °C for 120 min in a drying oven. Finally, the as-prepared samples were cooled at ambient temperature. A number of additional samples were prepared, following the same procedure. These samples were then submitted to higher temperatures of 260 °C, 300 °C, 340 °C and 380 °C in the drying oven, to further investigate the effect of temperature in superhydrophobicity.

### 2.3. Sample characterization

Surface morphologies were investigated by scanning electron microscopy (SEM, EVO18, ZEISS). Confocal Laser Scanning Microscope (CLSM, OLYMPUS OLS3000, Japan) was employed to analyze the surface roughness. The magnification in use was 240 times and the wavelength of semiconductor laser was  $408 \pm 5$  nm. The chemical state of the surfaces was studied by X-ray photoelectron spectroscopy (XPS, SPECS XR50, Japan). The surface wetting behavior was assessed by measuring the equilibrium contact angle (CA) with water, using a contact angle meter (DSA25, Germany). These measurements were performed using the sessile drop method at an ambient temperature of  $23 \pm 2$  °C and a relative humidity of  $53 \pm 5\%$ . Water droplets with a volume of 3  $\mu\text{L}$  were carefully deposited onto the surfaces in five different positions to obtain the average static contact angle value, as well as the sliding angle and the contact angle hysteresis. Thermogravimetry (TG) measurements were carried out making use of a thermal analysis system (DTA, SDT-Q600, TA Instruments Inc. USA) using a dynamic heating rate of  $10$  °C·min<sup>-1</sup> under N<sub>2</sub> protection conditions.

### 2.4. Characterization of anti-icing property

An apparatus composed of a recirculating cooling alcohol system (DFY-5/80 °C, YUEZHONG, China), an electronic temperature controller (SR93, SHIMADEN, Japan), a mechanical testing system (TES1310, ESM, China), an image acquisition system (HD Camcorder - LEGRIA HF R806, Canon, Japan) and a data collection system (DAQ11625, Quatronix, China) was assembled to characterize the anti-icing properties of the as-prepared samples, of which the inner wall was covered with thermal insulation material in order to keep the hermetic space temperature stable. Additionally, a high precision infrared thermometer (AS380, SMART, Hong Kong) was used in the investigation process.

#### 2.4.1. Ice adhesion strength and Ice shear strength investigation to the as prepared surfaces

The schematic diagram of the mechanical testing system is shown in Fig. 1a. The hermetic space temperature, monitored by an electronic temperature controller, was controlled at  $-30 \pm 2$  °C by the recycled water temperature controller. Before the force test, the as-prepared samples were fixed on the specimen stage by a mechanical clamping part. Afterward, a cylindrical container with the cross-section of 1 cm<sup>2</sup> was put on the sample surface and filled with water by a syringe. After freezing for 10 min, the ice column was due to form on the surfaces. The speed of the linear motion stage was controlled at 2 mm/s. After the ice column was completely departed from the surface, the peak values of thrust or pull were recorded by the acquisition system coupled with a personal computer. The ice adhesion strength and ice shear strength were obtained by averaging nine testing results.

#### 2.4.2. Freezing delay time investigation to the as prepared surfaces

The image acquisition system employed in this paper was the same used in our previously reported work [33]. The real-time temperature of hermetic space and specimen stage were collected by the electronic temperature controller, as shown in Fig. 1b. The relative humidity of the hermetic space was  $53 \pm 10\%$  [34], and the experimental temperature of the specimen stage and space was controlled at

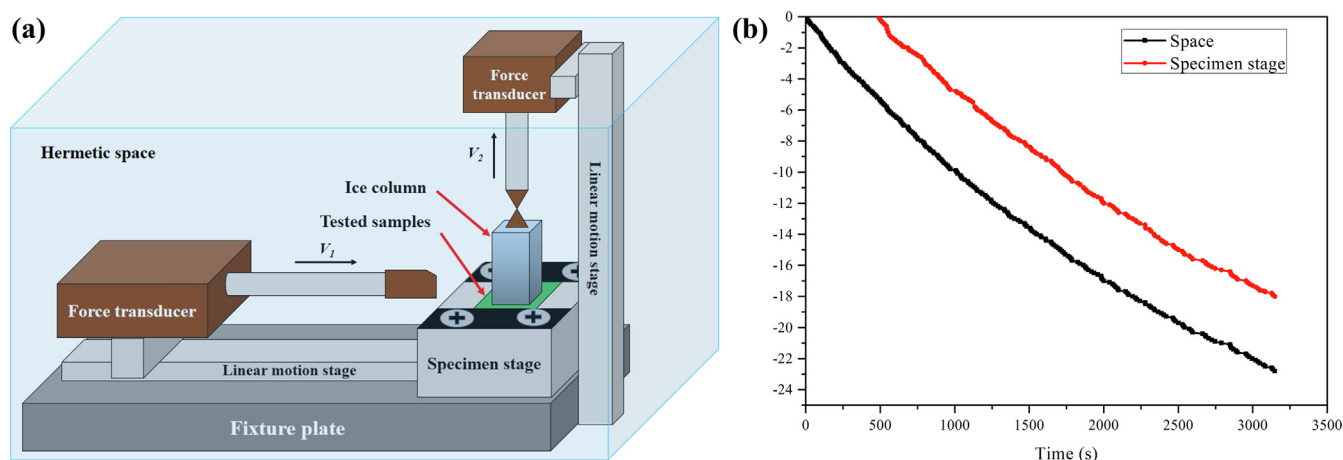


Fig. 1. (a) Schematic illustration showing the ice adhesion test apparatus; (b) Graph showing the relationship between time and temperature of experimental space and specimen stage.

$-9.5 \pm 1.5^\circ\text{C}$  and  $-11 \pm 1.5^\circ\text{C}$ , respectively. The reference water droplets ( $50\ \mu\text{L}$ ) were deposited on the sample surfaces, which was fixed on the specimen stage by mechanical components. The ice-nucleation triggered temperature (INTT) was also investigated when the experimental temperature of space and specimen stage decreased at  $0^\circ\text{C}$ . Both of the icing processes were monitored and recorded by the HD Camcorder.

#### 2.4.3. Dynamic wettability investigation of as-prepared surfaces at low temperature

The samples were placed in the tested chamber of our self-established apparatus for 1 min before the experiment and tilted at an angle of  $\theta = 5^\circ$ . The experimental conditions were imposed as a controlled ambient temperature of  $-25.3 \pm 3^\circ\text{C}$ , while the temperature of the sample surface was  $-13.2^\circ\text{C}$ , which was evaluated by the high precision infrared thermometer (AS380, SMART, Hong Kong). And the relative humidity of the hermetic space was  $53 \pm 10\%$  [34]. Afterward, a single water droplet with a diameter of 1.5 mm and a weight of 0.01 g was dropped on the cold as-prepared surfaces, with the velocities of 1.4 m/s and 1.98 m/s respectively. Droplets impact was recorded using the HD Camcorder.

#### 2.5. Characterization of de-icing property on the as-prepared surfaces

All the as-prepared substrates and the experimental platform were put in a refrigerator for 12 h to ensure they were completely cold. The substrates were then transferred onto the cooling experimental platform in air atmosphere when they were under experiment. A spoon of snow was put on the substrates immediately. The de-icing process was captured by the HD Camcorder. In addition, the icing/deicing test of the as-prepared surfaces was carried out. In this test, the as-prepared surfaces were fixed on the bottom of a beaker in which pure water was poured, following by placing the beakers in the tested chamber at the temperature  $-30 \pm 2^\circ\text{C}$  for 30 min. Once the water was completely iced, the beakers were taken out to room temperature. After the ice was melted, the water contact angle of the as-prepared surface was investigated.

### 3. Results and discussion

#### 3.1. Surface morphology and wettability

To better elucidate the relationship of the surface geometric structure with surface wettability, SEM images were used to investigate the morphologies of as-prepared surfaces. Fig. 2a and b show the SEM images of Surf-4 at different magnifications. From Fig. 2a, one may

confirm that nubble-protrusions in regular sequences were successfully fabricated by irradiation. The complex structure of a single protrusion should be attributed to the etching process with the  $\text{CuCl}_2$  aqueous solution. Under higher magnification, interestingly, one can observe that cauliflower-like microspheres were scattered on the structured surface, which is composed of dozens of interconnected thin flakes, as shown in the inset of Fig. 2b. The following annealing process did not cause any obvious changes in morphology, as shown in Fig. S1. To further investigate the changes in surface roughness under different annealing temperatures, Confocal Laser Scanning Microscope (CLSM) was employed. From Fig. S2, it can be seen that surface roughness of Surf-4 is around  $32\ \mu\text{m}$ , which is two orders of magnitude larger than that of the bare surface ( $R_a = 0.825\ \mu\text{m}$ ). Additionally, it is found that the surface roughness fluctuates around  $30\ \mu\text{m}$ , which proves the annealing temperature is not likely to alter the surface morphology.

However, all the as-prepared surfaces are superhydrophobic, especially Surf-4 with a water contact angle (WCA) of about  $155^\circ \pm 2^\circ$  and a sliding angle (WSA) of about  $5^\circ \pm 2^\circ$ , as shown in Fig. 2c. This should be ascribed to the presence of air cushion between the liquid-solid interfaces [35]. However, as preparation temperatures increased, the WCA decreased and the WSA increased gradually, as shown in Fig. 2d. From the thermogravimetric analysis of the PDMS in nitrogen, it can be seen that the polymer starts to lose mass at about  $300^\circ\text{C}$ , as shown in Fig. 2e. In a nitrogen atmosphere, the degradation occurs through depolymerization, leading to the decrease of surface superhydrophobicity [36]. From Fig. 2f, it is found that the wettability of Surf-4 turned from superhydrophobic to superhydrophilic (WCA is about  $0^\circ$ ) after the surface was heated at  $400^\circ\text{C}$  on a heating station. This resulting superhydrophilic surface was labeled as Surf-B. Amazingly, this superhydrophilic surface (i.e. Surf-B) recovered its superhydrophobic and high-adhesion properties (WCA =  $152^\circ \pm 2^\circ$ , WSA >  $90^\circ$ ) after exposure in the air with relative humidity 30% for 120 days (Surf-C). After an additional exposure in the air for 150 days, Surf-D presented low-adhesion properties (WSA was  $15^\circ \pm 3^\circ$ ). Even aged for such a long time, there is no obvious changes in WCA of Surf-4 and its WSA increased to be  $8^\circ \pm 3^\circ$  only, which is labeled as Surf-A. In addition, the changes in contact angle hysteresis (CAH), i.e., the difference between advancing contact angle (ACA) and receding contact angle (RCA) for different coatings matches well with the tendency of the WSA, as shown in Table 2 (see support info). The results support that the as-prepared superhydrophobic samples possess the effective recovery property after destroyed and good chemical stability at a long aging time. Furthermore, it can be seen from Fig. 3 that the surface of Surf-D acts like a silver mirror when viewed at a glancing angle, which is caused by the total reflectance of light at the air layer retained in the interface. This phenomenon effectively proves that the wetting state of the recovered

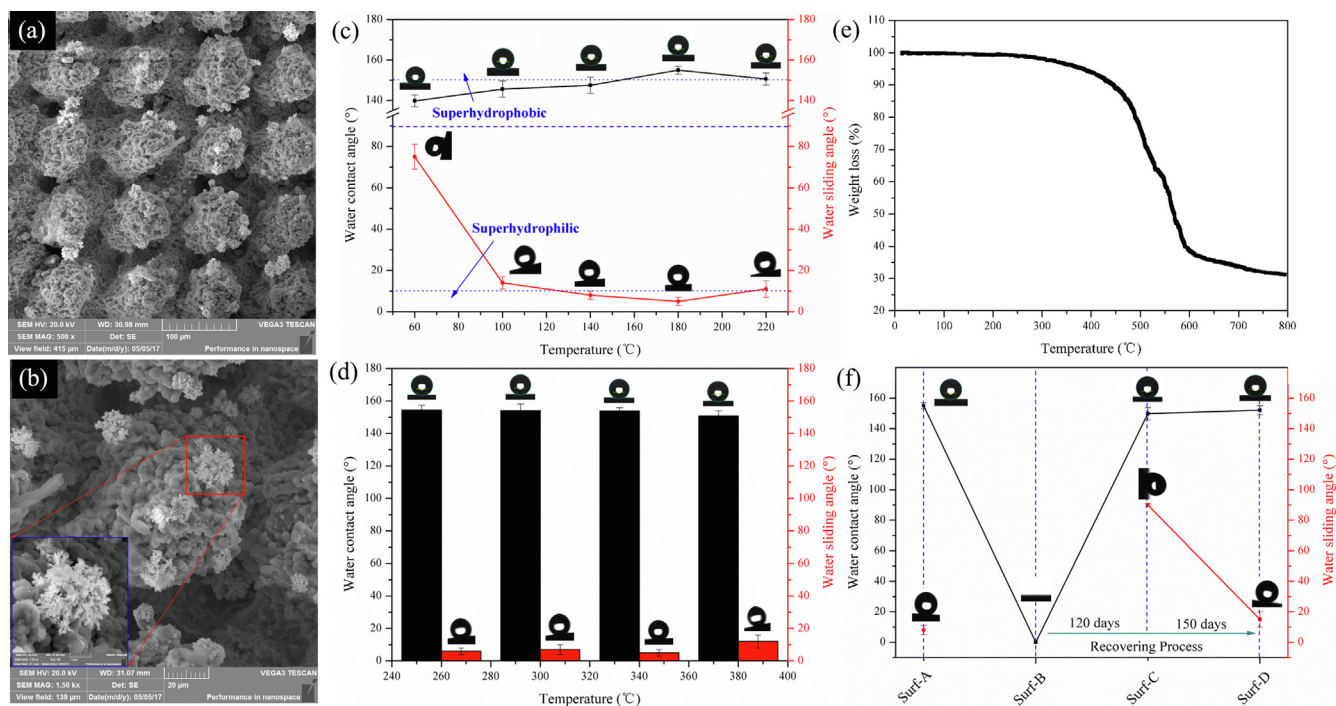


**Fig. 2.** SEM images of the as-prepared superhydrophobic surface heated by 180 °C: (a) low magnification SEM image (500 x) of surface panorama; (b) high magnification SEM image (1.5 kx) of one single micro-trabeculae; inset is high magnification SEM image (7.5 kx) of chrysanthemum-like structure on one single micro-trabeculae; (c) Wettability of as-prepared surfaces (surf-1 to surf-5) are reflected by water contact angle (WCA) and water sliding angle (WSA); (d) Wettability of as-prepared surfaces after heated at 260 °C, 300 °C, 340 °C and 380 °C; (e) The TGA thermograms of PDMS layer on the as-prepared surface; (f) Wettability changes of the surf-4 after heated at 400 °C and exposure for 120–150 days.

surface is the Cassie state [37].

### 3.2. Chemical characterization

Based on the results presented and discussed above, the X-ray photoelectron spectroscopy (XPS) was used to investigate the chemical composition evolution of the as-prepared surfaces in wettability transformation. Fig. 4a displays the XPS survey regions of the samples, containing strong signals of aluminum (Al), silicon (Si), copper (Cu), oxygen (O) and carbon (C). As shown in Fig. 4a, the peaks of elemental Cu, O, Al and C coexisted in all three samples, where the carbon peaks at 284.2 eV are attributed to the residual carbon from the sample and adventitious hydrocarbon from the XPS instrument itself. The peak with a binding energy of 74.25 eV is associated with Al 2p<sub>3/2</sub> emission [38]. The strong peak of Si at 102 eV was only observed on Surf-4. This proved that the molecular layer of PDMS was destroyed under the temperature of 380 °C (as shown in Fig. 2e), which led to the wettability transition from superhydrophobicity (Surf-4) to superhydrophilicity (Surf-B). It is found that a Cu2p doublet (Cu2p<sub>1/2</sub> and Cu2p<sub>3/2</sub>) at 930–955 eV, Cu3s at 120 eV, and Cu3p at 76 eV were shown in all three

samples, which should be attributed to the chemical displacement reaction of copper ion and aluminum, displayed as Scheme 1 (in support info). As the PDMS layer was destroyed under such a high temperature, the high-resolution spectra of O 1s and Cu 2p were detected for further analyzing the reasons of the wettability transition from superhydrophilicity (Surf-B) to superhydrophobicity (Surf-D). From Fig. 4b, the core level peaks Cu2p<sub>1/2</sub> and Cu2p<sub>3/2</sub> were recorded, and here only Cu 2p<sub>3/2</sub> is discussed because Cu 2p<sub>3/2</sub> and Cu 2p<sub>1/2</sub> play similar roles in determining the Cu valence. One can see from the inset of Fig. 4b that the peak at 933.6 eV is assigned to CuO, and the peak at 932.2 eV is related to low valence copper species (Cu<sup>0</sup>) [39,40]. As displayed in the inset of Fig. 4c, the O 1s region can be divided with two peaks; the peak at 530.7 eV is attributed to O<sup>2-</sup> of CuO species, and the peak at 531.9 eV is ascribed to O<sup>2-</sup> of Al<sub>2</sub>O<sub>3</sub> species [38]. During the oxidation process, the hydroxyl groups adsorbed on the defective sites can be replaced gradually by oxygen atoms [41]. The changes of atom percent shown in Table 1 (in support info) evidence that oxygen content in the surface oxide layer increases significantly, indicating that the native oxidation occurred during the exposure time of 150 days in ambient temperature. Thus, the observed transition from



**Fig. 3.** The mirror-like phenomenon can be observed on the recovered superhydrophobic sample submerged in water.

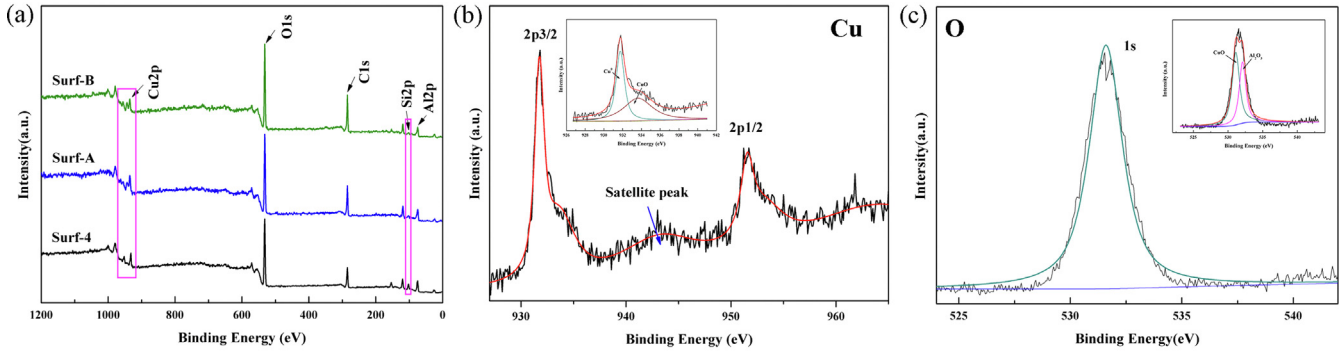


Fig. 4. The XPS survey spectrum of the chemical composition on the as-prepared surfaces. (a) Full spectrum. (b) The high-resolution spectra of Cu 2p; Inset is the fitting peak of Cu 2p<sub>3/2</sub>. (c) The high-resolution fitting spectra of O 1s regions of Surf-D; Inset is the fitting peak of O 1s.

superhydrophilicity to superhydrophobicity of the as-prepared surface should be attributed to the oxygen adsorption [42,43].

### 3.3. Anti-icing properties

Typically, excellent anti-icing performance of surfaces is associated to two main characteristics: i) how easy the deposited iced water droplets can be removed from the surfaces, or ii) the crystallization time of the water droplets is profoundly delayed under frozen conditions. To evaluate the anti-icing properties of as-prepared surfaces, both ice removing difficulty and the freezing delay time were evaluated. The apparatus developed in-house, as explained in Section 2, was employed to further examine the ice adhesion and shear strength on the tested surfaces. As shown in Fig. 5a, ice adhesion strength (IAS) of bare surface (B-surf) is  $191 \pm 10$  kPa. Surf-B (the superhydrophilic surface) exhibits the largest ice adhesion strength, which is  $868 \pm 43$  kPa. In contrast, the IAS of the Surf-4 (the superhydrophobic surface) is  $125 \pm 6$  kPa, which is obviously lower than B-Surf and eight times lower than Surf-B. Theoretically, the wetting state of liquids on surfaces can be described either by the Cassie-Baxter state or by the Wenzel state. For the Cassie-Baxter state, air trapped in the hierarchical structures of surfaces' topography forms a composite and intermittent solid-liquid-air three-phase contact line, resulting in a larger contact angle. Under frozen conditions, the work of adhesion between the ice and substrate surfaces depends on the release of elastic energy from the crack formation, which is formulated in Griffith's condition for crack initiation and scales as:[44]

$$R_{cr} = \frac{8 E^* \Delta\gamma_{i-s}}{\pi \sigma_{th}^2} \quad (1)$$

where  $R_{cr}$  is the radius of the interfacial contact area between ice and

substrate,  $\sigma_{th}$  is the theoretical adhesion strength,  $\Delta\gamma_{i-s}$  is the work of adhesion between the ice and substrate, and the combined Young's modulus  $E^*$  is defined as:[44]

$$\frac{1}{E^*} = \frac{1 - \nu_i^2}{E_i} + \frac{1 - \nu_s^2}{E_s} \quad (2)$$

where  $E_i$  and  $\nu_i$  are Young's modulus and Poisson's ratio of ice, and  $E_s$  and  $\nu_s$  are Young's modulus and Poisson's ratio of the solid substrate. If the crack area is recognized as same as the effective specific surface area (SSA): [45]  $SSA = \pi R_{cr}^2$ , the Eq. (1) can be transformed into

$$\Delta\gamma_{i-s} = \frac{\pi \sigma_{th} \sqrt{SSA}}{8 E^*} \quad (3)$$

Thus, the interfacial adhesion of ice and substrate is proportional to SSA.

As the trapped air provides more space for the deformation of iced water, the iced water is not going to penetrate the air cushion completely and mechanically interlock [46]. In this situation, the contact relationship between ice and the solid surface is identified as contact point, as shown in Fig. 5b. Here, the efficient specific surface area of the as-prepared superhydrophobic surface can be quantified as:

$$SSA_C = n\pi r^2 + 2\pi r \sum_{i=1}^n L_i + \xi_C \quad (4)$$

where  $r$  is the radius of each micro-nano pillar,  $L_i$  is the ice-covered length of each micro-nano pillar,  $n$  is the number of the ice-covered micro-nano pillars,  $\xi_C$  is the parameter of area compensation of as-prepared superhydrophobic surface. Comparing with the superhydrophobic surface, the contact relationship of the smooth surface and superhydrophilic surface between ice and solid surface are identified as contact area. The efficient specific surface area of the smooth surface

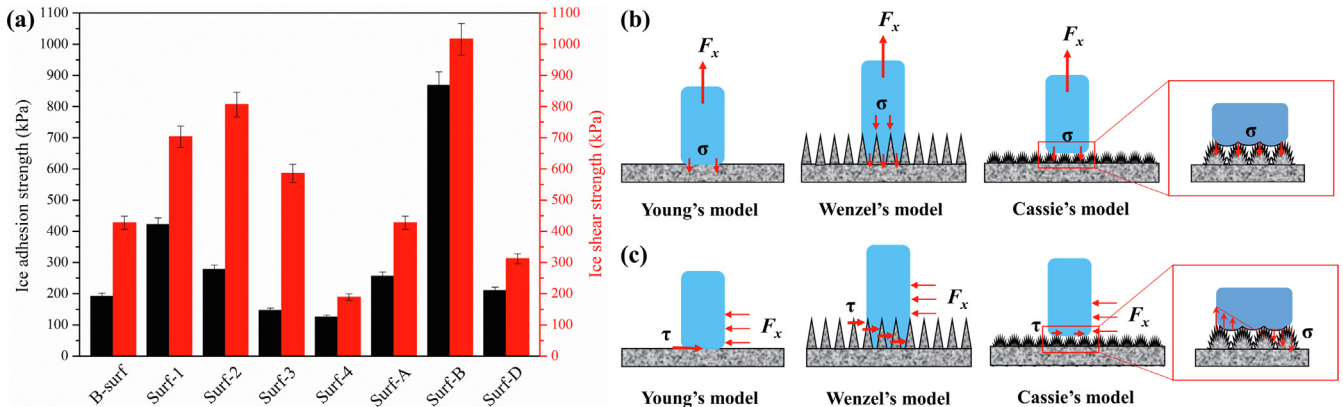
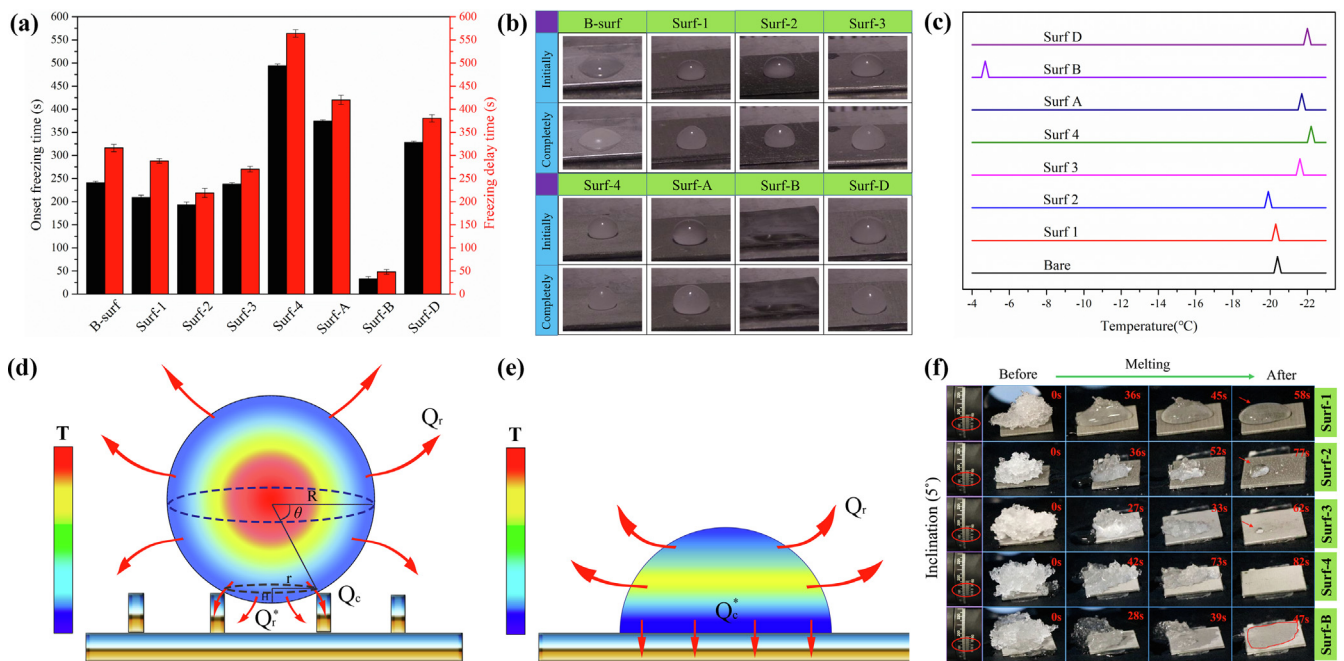


Fig. 5. (a) Ice adhesion strength and ice shear strength of as-prepared surfaces; (b) The mechanism of ice adhesion strength test on different wettability surfaces; (c) The mechanism of ice shear strength test on different wettability surfaces.



**Fig. 6.** (a) Statistical data of the freezing delay time and the freezing finish time on as-prepared surfaces; (b) The situ observation of the water droplets on the as-prepared surfaces; (c) The ice-nucleation triggered temperature (INTT) of the as-prepared surfaces; (d) The heat transfer model of water droplets on superhydrophobic surface; (e) The heat transfer model of water droplets on bare surface; (f) The situ observation of deicing process on the as-prepared surfaces.

can be quantified as:

$$SSA_Y = \pi R_{cr}^2 + \xi_Y \quad (5)$$

where  $R_{cr}$  is the radius of the ice-covered area of the smooth surface and  $\xi_Y$  is the parameter of area compensation of as-prepared smooth surface. However, the textured surface was filled with iced water under the action of capillary forces and completely connected with the substrate. Therefore, the efficient specific surface area of the superhydrophilic surface can be quantified as

$$SSA_W = \pi R_{cr}^2 + 2n\pi rL + \xi_W \quad (6)$$

where  $L$  and  $\xi_W$  are the height of each micro-nano pillar and the parameter of area compensation of the as-prepared superhydrophilic surface, respectively. Since the as-prepared surface structures do not depict the optimal shapes,  $\xi_C$ ,  $\xi_Y$  and  $\xi_W$  are introduced to compensate the efficient specific surface area. From the analysis above, it can be concluded that the specific surface area of the different wettability surface is  $SSA_W > SSA_Y > SSA_C$ .

On the other hand, the as-prepared superhydrophobic surface exhibited excellent water-repellent property because the substrate was covered by a layer of molecules with non-polar groups. Therefore, the main IAS was contributed by the physical adhesion ( $\sigma_{adh}$ , per unit area) between the ice-solid interfaces after the water was iced on the surface. However, the polar groups were completely exposed on the as-prepared surface once the superhydrophobic layer was destroyed at high temperature. At this situation, removal of the ice from the as-prepared superhydrophilic surface not only needs to overcome the adhesive strength  $\sigma_{adh}$  between the ice-solid interface, but also the orientation force ( $\sigma_{ori}$ , per unit area) between polar molecules, which is much bigger than the adhesive strength. As to the bare surface, the surface oxide layer can also greatly diminish the orientation force of the interface, the IAS of which is mainly attributed to the physical adhesion  $\sigma_{adh}$ . Thus, the relationship of the IAS on different wetting surfaces is that  $\sigma_W (\sigma_{adh} + \sigma_{ori}) > \sigma_Y = \sigma_C (\sigma_{adh})$ . Based on the mechanical formula  $F = \sigma \cdot SSA$ , it can be concluded that the external force exerted on the ice column is  $F_W > F_Y > F_C$ , which is in good agreement with the numerical data tested in our in-house developed apparatus.

In addition, the ice shear strength (ISS) measured for Surf-4 (the superhydrophobic surface) is  $189 \pm 10$  kPa, which is two times lower than that obtained in B-surf ( $428 \pm 21$  kPa) and five times lower than that measured for Surf-B ( $1016 \pm 51$  kPa), as shown in Fig. 5a. Moreover, the IAS and ISS of Surf-A are  $256 \pm 13$  kPa and  $428 \pm 21$  kPa, respectively. Both of them are larger than those obtained for Surf-4, which should be attributed to the contamination of Surf-4 during the storage. However, the IAS and ISS of Surf-D are  $210 \pm 11$  kPa and  $312 \pm 16$  kPa respectively, both of which are smaller than those obtained for Surf-B. Hence, these results show that the restored superhydrophobic surface can still decrease the ice adhesion and shear strengths and exhibit excellent anti-icing properties. Comparing with the detachment mechanism of IAS test, the detachment mechanism of ISS test is complex and different, as shown in Fig. 5c. When the external force was exerted on the ice column, the interfacial shear ( $\tau$ ) and tensile ( $\sigma$ ) stresses are acting on Surf-4 simultaneously, which can be defined as:

$$F_C = \lambda \pi R_{cr}^2 \tau_i + (1 - \lambda) SSA_C \sigma_{th} \quad (7)$$

where  $\lambda$  is the area fraction of shear deformation area and  $\tau_i$  is the theoretical shear strength of ice. As to the Surf-B, the removal of ice needs to overcome the adhesive strength between the ice and substrate as well as the cohesive strength due to the mechanical interlocking, which can be defined as:

$$F_W = n\pi r^2 \tau_{i-s} + (R_{cr}^2 - nr^2) \pi \tau_i \quad (8)$$

where  $\tau_{i-s}$  is the theoretical shear strength of the ice-solid interface. However, the removal of ice on B-surf only needs to overcome the adhesive strength between the ice and the substrate, which can be defined as:

$$F_Y = \pi R_{cr}^2 \tau_{i-s} \quad (9)$$

From this analysis, it can be concluded that the surface wettability, as described in Fig. 5b and c, governs the interfacial contact form between ice and substrate. Therefore, the as-prepared superhydrophobic surface can greatly reduce the ice adhesion and shear strengths and be potentially applied in different fields.

Conventionally, the freezing delay time is defined as the time interval from the cooling start to the freezing start. However, the initial ambient temperature will significantly impact the freezing delay time, which results in the experimental freezing delay time deviating from actual values of freezing delay time. Under thermodynamic equilibrium conditions, the freezing temperature of pure water is 0 °C. If the ambient temperature keeps decreasing, the pure water will lose its fluidity and adhere to the surface in the form of ice. Thus, the ambient temperature is also needed to be controlled for the investigation of the freezing delay time. As shown in Fig. 6a, two parameters were recorded, namely the onset freezing time and the freezing delay time. The onset of freezing time is the time interval required for the deposited water droplets to become opaque, while the freezing delay time is the time when the icing process finishes with the outline changes of ice. The recorded data demonstrated that the water droplet on the B-surf cooled rapidly, and the water droplet became opaque at 241 s and frozen at 316 s. Water droplets on the Surf-4, Surf-A and Surf-D take a longer time to completely freeze, especially the droplets on the Surf-4 (564 s), for which the onset freezing time is 494 s. However, water droplets spread quickly and froze on the textured surface at 48 s. From the in-situ observation displayed in Fig. 6b, the water droplets on the as-prepared superhydrophobic surfaces remained in a semi-sphere form at the onset of the freezing process and transformed into peach-like shape after freezing completely. However, no obvious changes were found on the as-prepared superhydrophilic surface where an ice film is formed. Meanwhile, it is observed that the transparency of water droplets kept decreasing during the icing process when the nucleation was triggered.

In general, the state of matter is determined by the competition between the thermal motion of molecules and the interaction between molecules. The thermal motion of a liquid molecule manifests itself as vibration at one location and then at another location. As the temperature continues to drop, the liquid will solidify and turn into a solid phase. The thermal motion of a molecule in the solid phase can only vibrate at a fixed position, which is more orderly than that occurring in the liquid state. When the temperature drops below the critical temperature  $T_c$ , solid nuclei begin to form in the liquid phase where the stable phase is the solid phase. Therefore, the onset freezing temperature was investigated when the experimental temperature of space and specimen stage decreased at 0 °C. During this test, the experimental temperature of space and specimen stage presented linear variations with time, as shown in Fig. 1b. Fig. 6c shows that ice nucleation on B-surf was triggered when the water droplets cooled to -20.4 °C. On Surf-4, Surf-A, and Surf-D, the ice-nucleation triggered temperature (INTT) decreased further with respect to the B-surf, especially the INTT on Surf-4, which decreased to -22.2 °C. Markedly, there is a different phenomenon observed on the Surf-B, with the ice-nucleation triggered temperature of -4.7 °C. The results show that the recovered superhydrophobic surface is still able to prolong the freezing time and decrease the icing temperature. The different mechanisms of the icing process can be analyzed by a simplified specific heat transfer model. As shown in Fig. 6d, water droplets were suspended over the textured superhydrophobic surface due to the existence of the air cushion below. It should be noted that there are three main terms contributing to the heat loss, i.e. the heat conduction between the water–solid interface, heat radiation between the water and air cushion and the convective heat transfer between the water and the air of hermetic space [47,48]. So this heat transfer system can be defined, according to a simple energy balance, as:

$$\Delta Q = Q_c + Q_r + Q_r^* \quad (10)$$

where  $\Delta Q$  is the total heat loss in the icing process;  $Q_c$  is the heat power lost by conduction;  $Q_r$  is the heat power lost by natural convection;  $Q_r^*$  is the heat power lost by thermal radiation of gas-liquid contact between the three-phase interface.

Based on the Fourier's law, Newton's law of cooling and Stefan-Boltzmann law, the equation of heat transfer process can be described

as:

$$\begin{aligned} \Delta Q_c = & \alpha \cdot 2\pi R^2 (1 + \sin \beta) (T_d - T_s) \\ & + C_n \cdot 2\pi R^2 (1 - \sin \beta) \left[ \left( \frac{T_d}{100} \right)^4 - \left( \frac{T_{sub}}{100} \right)^4 \right], \\ & + \lambda \cdot SSA_C \cdot \left( \frac{T_d - T_{sub}}{x} \right) \end{aligned} \quad (11)$$

where  $\alpha$  is the convective heat transfer coefficient;  $C_n$  is the radiation heat transfer coefficient;  $\lambda$  is the thermal conductivity of the aluminum alloy;  $R$  is the radius of the sphere;  $T_a$  is the real-time hermetic space temperature;  $T_d$  is the initial temperature of the droplet;  $\beta$  is the contact angle of a droplet (CA);  $x$  is the thickness of the substrates.

Therefore, the heat loss rate ( $\eta_c$ ) of a water droplet on superhydrophobic surface during the icing process can be identified as:

$$\eta_c = \frac{\Delta Q_c}{t_c} \quad (12)$$

However, there is no trapped-air on the bare surface and thus liquid-solid contact area is much larger than that of the superhydrophobic surface, as shown in Fig. 6e. Under these conditions, Eq. (11) should be re-defined as:

$$\Delta Q_Y = Q_r + Q_c = \alpha \cdot 2\pi R^2 (1 - \sin \beta) (T_d - T_s) + \lambda \cdot SSA_Y \cdot \left( \frac{T_d - T_{sub}}{x} \right). \quad (13)$$

The heat loss rate ( $\eta_Y$ ) of water droplet on bare surface during the icing process can be identified as:

$$\eta_Y = \frac{\Delta Q_Y}{t_Y} \quad (14)$$

Based on the parameters in Table 3 (see support info), the heat loss rate on the superhydrophobic surface and the bare surface can be calculated as:  $\eta_c = 6.59 \times 10^{-3}$  J/s. (Here, the  $SSA_C$  was recognized in the ideal situations that water droplet was completely suspended on the microstructure, i.e.:  $SSA_C = \pi r r^2$ ),  $\eta_Y = 2.52 \times 10^{-2}$  J/s. As a result, the heat loss rate of the water droplet on a superhydrophobic surface is an order of magnitude larger than that on the bare surface during the icing process. On the other hand, the heat conduction between the liquid-solid interfaces is the main form of heat loss of water droplet. Therefore, surface wettability is the dominant factor in the surface icing delay performance. That is the reason why the hierarchical superhydrophobic surface can significantly prolong the freezing time and decrease the ice-nucleation triggered temperature.

Besides the anti-icing property, the de-icing property is another advantage of ice-phobic surfaces. The de-icing performance of the as-prepared surfaces was also investigated, as shown in Fig. 6f (See Section 2.5 for the description of the testing procedure). The specimen stage was fixed at 5°. It is found that the snow was gradually melted expand on the Surf-1, and the melted water finally stuck on the textured surfaces. The same phenomenon was found on Surf-2 and Surf-3, due to parts of water droplets intruded and stocked in the gaps of the surface due to the action of capillary forces. Regarding Surf-4, the air cushion between the liquid-solid interfaces prevented the water penetrating into the textured surfaces, which promotes water sliding off the surfaces. Obviously, Surf-B was completely wetted by melted water. Once the ambient temperature decreased to the critical temperature, the stocked water was definitely frozen to be the ice film. In addition, it is found that the water contact angle of Surf-4 fluctuated at 151° after 10 times of the icing/deicing test, as shown in Fig. S4. Although the water contact angle of Surf-D was decreased in small scale after 10 times of the icing/deicing test, it still presented good superhydrophobic property. Therefore, the as-prepared superhydrophobic surfaces also exhibit an excellent de-icing property, which can be widely applied in many fields.

Several authors have published in the open literature a significant amount of data showing that the glaze ice from freezing rain can cause

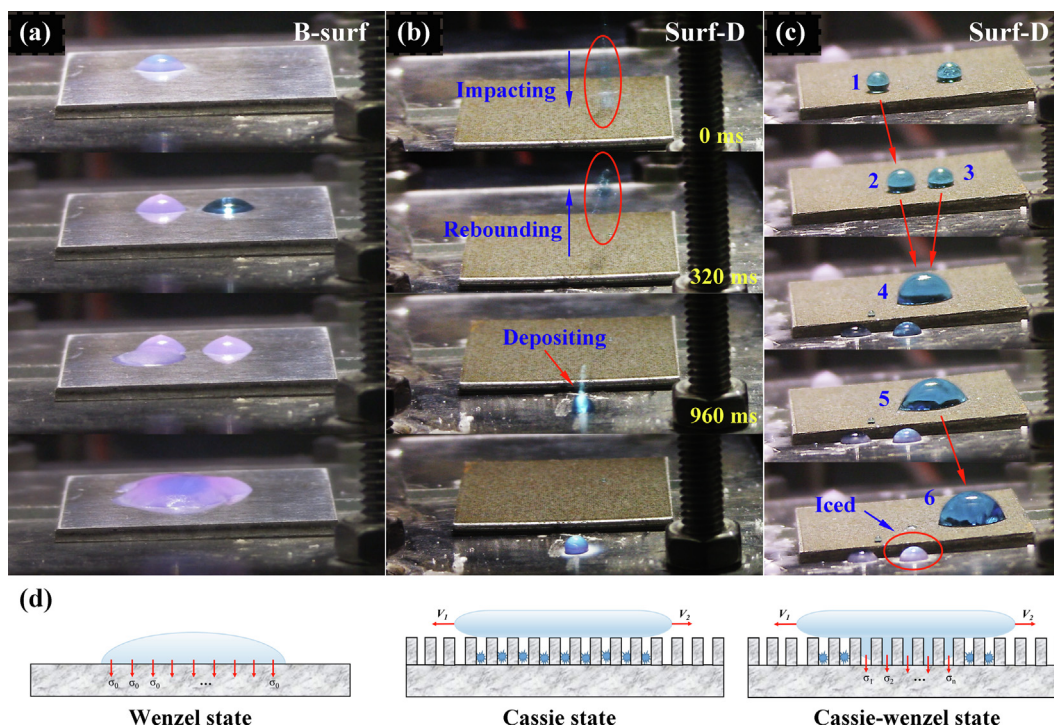


Fig. 7. Dynamic processes of water droplets impacting on the bare surface (a) and the recovered superhydrophobic surface at different velocities (b) 1.4 m/s and (c) 1.98 m/s. (d) Schematic of impacting process of water droplets in above three situations.

very rapid structural icing on aircraft by changing the shape of its airfoils. So, water dropping test was employed to evaluate the anti-icing property of samples. The diameter of a single water droplet is about 1.5 mm and its weight is about 0.01 g. The samples were placed in the tested chamber of our apparatus developed in-house for 1 min before the investigation and tilted at an angle of  $\theta = 5^\circ$  (as described in 2.4). The experimental conditions were imposed as a controlled ambient temperature of  $-25.3 \pm 3^\circ\text{C}$ , while the temperature of the sample surface was  $-13.2^\circ\text{C}$ , which was evaluated by the high precision infrared thermometer. As can be seen from Fig. 7a, water droplets were frozen quickly once dropped on the bare surface. Gradually, the bare surface has already been covered with a dense layer of ice in 22.78 s (see Supporting Information Video 1). However, water droplet completely bounced off from the recovered superhydrophobic surface and deposited on the cold experimental platform. In this case, the water droplet was released at the position of 15 cm high, so the impacting velocity ( $V_0$ ) could reach up to 1.4 m/s. It takes 320 ms from the impacting process to rebounding process and 960 ms from the rebounding process to the depositing process (see Supporting Information Video 2). Obviously, the second stage takes more time than the first stage, which demonstrates that the motion of water droplet is a ramp parabolic movement after it bounced off from the surface. The movement time of water droplets can be defined as  $t_m = \frac{2V_1 \cos 2\theta}{g}$ . Indirectly one can get the rebounding velocity of the water droplet, i.e.  $V_1 = 0.48$  m/s. Therefore, based on the first law of thermodynamics, the energy loss of impacting process is  $W_1 = 8.65 \times 10^{-6}$  J, which should be ascribed to two main energy loss, i.e. thermal energy loss and mechanical energy loss. If the released height of water droplet was increased to 20 cm, the impacting water droplets, as shown in Fig. 7c, were stuck on the recovered superhydrophobic surface in the shape of a ball because parts of the air cushion were penetrated by the high-speed water. In this situation, the impacting velocity of the water droplet is about 1.98 m/s. During this process, the energy loss can be calculated as  $W_2 = 19.6 \times 10^{-6}$  J, which is two times larger than  $W_1$ . Moreover, it was found that two of the water droplets jumped off from the surface and iced on the experimental platform. The above phenomenon can be well explained by

conventional wettability model, as shown in Fig. 7d. The aggregated droplets in Wenzel state cannot move because of the large adhesion force  $\sigma_0$  between the liquid and the bare surface. When the water droplets impact on the superhydrophobic surface at low velocities, the air cushion on the surface is still able to hold the water droplets instead of stick on the surface, indicating the surface remains in the Cassie state even at such low temperature. However, once water droplet in high velocity penetrates the air cushion on the surface, it will completely contact with the micro-scale ice in the micro-nano structure which is formed by the frozen water molecules in the air. So this impacting process greatly increases the interface area for energy dissipation and leads to a large amount of energy loss [49]. The wetting state of this situation is defined as “Cassie - Wenzel state”. Therefore, it can be concluded that the Wenzel state and the “Cassie - Wenzel state” should be completely avoided in the anti-icing process by increasing the depth and decreasing the width of the micro-gaps at a certain ratio. Amazingly, it is found that the stuck water droplet spontaneously moved from position 1 to position 2, when another water droplet collided with it (see Supporting Information Video 3). At the same time, the two water droplets merged into a bigger one and stuck at position 2. Keep dropping the water droplets in a certain direction, the stuck water droplet became bigger and bigger and gradually moved from position 1 to position 6. It should be noted that the directional water droplets movement was triggered by another impacting water droplets. At such a high impacting velocity, parts of the water droplet stuck on the surface, which acted as a center and drove the former water droplet moving and coalescing together. In other words, it also proved the low adhesion strength between the water droplets and the cold substrates. This phenomenon suggests that water droplets can be directionally transferred from one place to another if the temperature of substrates and the velocity of water droplets are precisely controlled.

The self-cleaning property of a superhydrophobic surface is very important for its applications, which can effectively protect it from the potential contaminations of the environment, especially at low temperature. Here, the self-cleaning performance of Surf-D was demonstrated with outdoor soil of our campus as a model contaminant. As

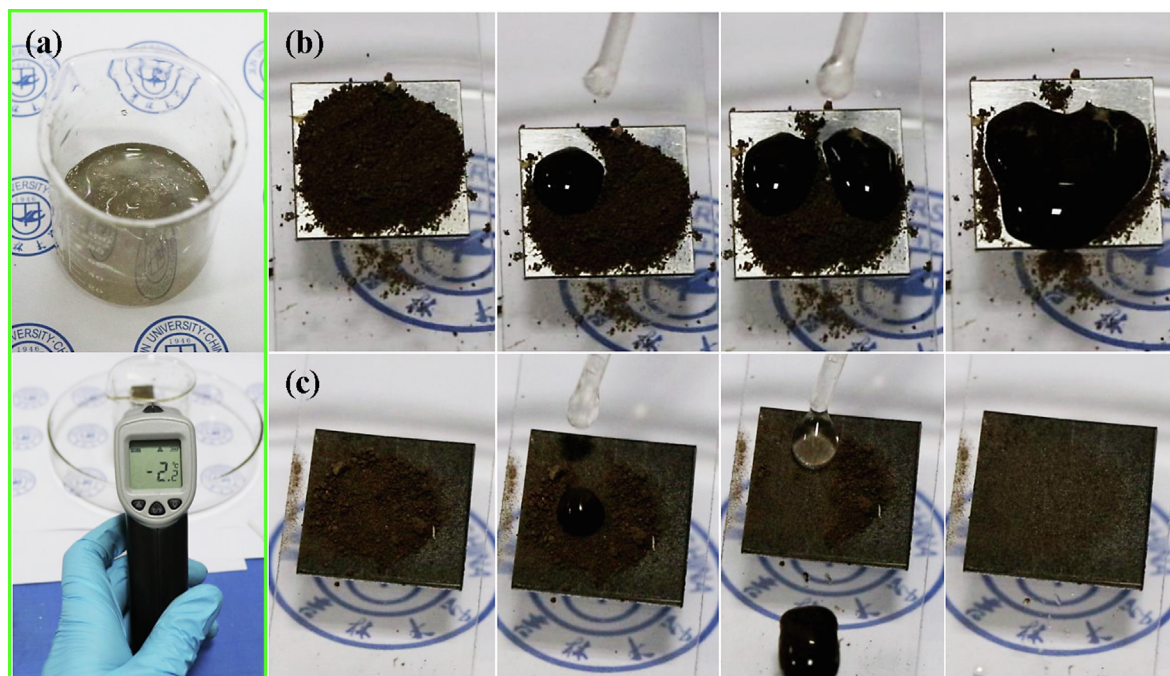


Fig. 8. (a) The super-cold water with temperature of  $-2.2\text{ }^{\circ}\text{C}$ ; (b) and (c) Self-cleaning process of the B-surf and the Surf-D respectively.

shown in Fig. 8b and c, layers of outdoor soil were sprinkled on the B-surf and Surf-D respectively. In order to test the self-cleaning property of recovered superhydrophobic surfaces at low temperature, the super-cold water with temperature of  $-2.2\text{ }^{\circ}\text{C}$  was chosen to be the cleaning liquid, as shown in Fig. 8a. As water droplets were dropped on the contaminated B-surf, the water droplets quickly swallowed the surrounding soil and stuck on the surface, as shown in Fig. 8b. Unfortunately, the B-surf was fully covered by mud. However, it can be seen from Fig. 8c that the soil on Surf-D was immediately picked up and carried away by the super-cold water droplets, leaving behind a clear surface. This phenomenon should be attributed to the trapped-air in the microstructure [50] and the high capillary force of the water droplet [51]. Therefore, the recovered superhydrophobic surfaces also present excellent self-cleaning property and can be potentially applied in the polluted environment at low temperature.

#### 4. Conclusion

In summary, superhydrophobic surfaces with a static water contact angle of  $155^{\circ} \pm 2^{\circ}$  and a sliding angle of  $5^{\circ} \pm 2^{\circ}$  were manufactured from an aluminum alloy by combining laser-fabrication and chemical etching processes, followed with chemical vapor deposition of PDMS. Superhydrophobic surfaces turn to superhydrophilic when submitted to high temperatures ( $T > 400\text{ }^{\circ}\text{C}$ ), but recover then the Cassie state, when exposed to air, as confirmed by the silver mirror effect. The XPS analysis showed that the transformation from superhydrophilicity to superhydrophobicity should be attributed to the oxidization of copper that is present in the alloy. From the evaluation of the ice adhesion and shear strengths, the superhydrophilic surface exhibited the worst ice removing property, but the ice adhesion strength (IAS) and the ice shear strength (ISS) of the recovered superhydrophobic surface were obviously lower than those obtained for bare surface and superhydrophilic surface. The results show that ice adhesion strength on different wettability surfaces strongly depends on the efficient specific surface area of the ice-solid interface. Due to the different situations of the solid-liquid-air three-phase contact line, the efficient specific surface area on the superhydrophobic surface is smaller than for a smooth surface and superhydrophilic surface, i.e.  $SSA_W > SSA_Y > SSA_C$ . Additionally, based on three mechanical equations of the ice shear strengths, it can be

concluded that the surface wettability governs the interfacial contact form between ice and substrate. From the recorded data of freezing delay time and icing temperature, the recorded superhydrophobic surface displayed better performance than the B-surf and superhydrophilic surface. Employing a specific heat transfer model, the different mechanisms of the icing process were thoroughly analyzed, which indicates that the air cushion can inhibit the heat transfer of liquid-solid interface under cold conditions. The study on the impact dynamics of water droplets on the recovered superhydrophobic surface at low temperatures indicates that it is important to keep Cassie state by increasing the depth and decreasing the width of the micro-gaps at a certain ratio. Also, the air cushion on the recovered superhydrophobic surface can prevent the melted water from secondary icing and potential contaminations, especially at low temperature. Consequently, we thoroughly investigated the anti-/de-icing properties of the recovered superhydrophobic surface and offered fundamental insights on the ice removing mechanism and heat transfer process.

#### Declaration of Competing Interest

The authors declared that there is no conflict of interest.

#### Acknowledgements

Authors are grateful to the National Key Research and Development Program of China (No. 2016YFE0132900). Fundação para a Ciência e Tecnologia (FCT) for partially financing the research under the framework of the project JICAM/0003/2017, in the context of Projecto 3599 - Promover a Produção Científica, o Desenvolvimento Tecnológico e a Inovação. A.S. Moita also acknowledges FCT for the IF 2015 recruitment program (IF 00810-2015) and exploratory project associated with this contract.

#### Appendix A. Supplementary data

Supplementary data to this article can be found online at <https://doi.org/10.1016/j.apsusc.2019.144386>.

## References

- [1] R. Gent, N. Dart, J. Cansdale, Aircraft icing, *Philos. T. R. Soc. A* 358 (2000) 2873–2911.
- [2] N. Dalili, A. Edrissy, R. Carriveau, A review of surface engineering issues critical to wind turbine performance, *Renew. Sust. Energy Rev.* 13 (2009) 428–438.
- [3] G. Isaac, S. Cober, J. Strapp, A. Korolev, A. Tremblay, D. Marcotte, Recent Canadian research on aircraft in-flight icing, *Can. Aeronaut. Space J.* 47 (2001) 213–221.
- [4] A. Kirillova, L. Ionov, I.V. Roisman, A. Synytska, Hybrid Hairy Janus particles for anti-icing and de-icing surfaces: synergism of properties and effects, *Chem. Mater.* 28 (2016) 6995–7005.
- [5] Q. Li, Z. Guo, Fundamentals of icing and common strategies for designing biomimetic anti-icing surfaces, *J. Mater. Chem. A* 6 (2018) 13549–13581.
- [6] K. Han, T.Y. Park, K. Yong, H.J. Cha, Combinational biomimicking of lotus leaf, mussel, and sandcastle worm for robust superhydrophobic surfaces with biomedical multifunctionality: antithrombotic, antibiofouling, and tissue closure capabilities, *ACS Appl. Mater. Interf.* 11 (2019) 9777–9785.
- [7] S. Dai, Y. Zhu, Y. Gu, Z. Du, Biomimetic fabrication and photoelectric properties of superhydrophobic ZnO nanostructures on flexible PDMS substrates replicated from rose petal, *Appl. Phys. A* 125 (2019).
- [8] F. Bai, J. Wu, G. Gong, L. Guo, Biomimetic “water strider leg” with highly refined nanogroove structure and remarkable water-repellent performance, *ACS Appl. Mater. Interf.* 6 (2014) 16237–16242.
- [9] H. Zhao, S.J. Park, B.R. Solomon, S. Kim, D. Soto, A.T. Paxson, K.K. Varanasi, A.J. Hart, Synthetic butterfly scale surfaces with compliance-tailored anisotropic drop adhesion, *Adv. Mater.* 31 (2019) e1807686.
- [10] J. Lv, Y. Song, L. Jiang, J. Wang, Bio-inspired strategies for anti-icing, *ACS Nano* 8 (2014) 3152–3169.
- [11] Y. Zhuo, V. Hakonsen, Z. He, S. Xiao, J. He, Z. Zhang, Enhancing the mechanical durability of icephobic surfaces by introducing autonomous self-healing function, *ACS Appl. Mater. Interf.* 10 (2018) 11972–11978.
- [12] S. Sun, L. Zhu, X. Liu, L. Wu, K. Dai, C. Liu, C. Shen, X. Guo, G. Zheng, Z. Guo, Superhydrophobic shish-kebab membrane with self-cleaning and oil/water separation properties, *ACS Sustain. Chem. Eng.* 6 (2018) 9866–9875.
- [13] N. Wang, L. Tang, W. Tong, D. Xiong, Fabrication of robust and scalable superhydrophobic surfaces and investigation of their anti-icing properties, *Mater. Des.* 156 (2018) 320–328.
- [14] D. Li, Z. Guo, Metal-organic framework superhydrophobic coating on Kevlar fabric with efficient drag reduction and wear resistance, *Appl. Surf. Sci.* 443 (2018) 548–557.
- [15] W. Tong, D. Xiong, N. Wang, C. Yan, T. Tian, Green and timesaving fabrication of a superhydrophobic surface and its application to anti-icing, self-cleaning and oil-water separation, *Surf. Coat. Technol.* 352 (2018) 609–618.
- [16] S.F. Ahmadi, S. Nath, G.J. Iliff, B.R. Srijanto, C.P. Collier, P. Yue, J.B. Boreyko, Passive antifrosting surfaces using microscopic ice patterns, *ACS Appl. Mater. Interf.* 10 (2018) 32874–32884.
- [17] H.A. Stone, Ice-phobic surfaces that are wet, *ACS Nano* 6 (2012) 6536–6540.
- [18] I. Castaneda-Montes, A.W. Ritchie, J.P.S. Badyal, Atomised spray plasma deposition of hierarchical superhydrophobic nanocomposite surfaces, *Colloid. Surf. A* 558 (2018) 192–199.
- [19] W. Liu, F. Sun, L. Jiang, J.C. Meredith, Y. Deng, Surface structure patterning for fabricating non-fluorinated superhydrophobic cellulosic membranes, *ACS Appl. Polym. Mater.* 1 (2019) 1220–1229.
- [20] L. Hou, N. Wang, J. Wu, Z. Cui, L. Jiang, Y. Zhao, Bioinspired superwettability electrospun micro/nanofibers and their applications, *Adv. Funct. Mater.* 28 (2018) 180114.
- [21] M. Yang, W. Liu, C. Jiang, S. He, Y. Xie, Z. Wang, Fabrication of superhydrophobic cotton fabric with fluorinated TiO<sub>2</sub> sol by a green and one-step sol-gel process, *Carbohydr. Polym.* 197 (2018) 75–82.
- [22] Y. Zhao, Z. Xu, X. Wang, T. Lin, Photoreactive azido-containing silica nanoparticle/polycation multilayers: durable superhydrophobic coating on cotton fabrics, *Langmuir* 28 (2012) 6328–6335.
- [23] L. Yin, Y. Wang, J. Ding, Q. Wang, Q. Chen, Water condensation on superhydrophobic aluminum surfaces with different low-surface-energy coatings, *Appl. Surf. Sci.* 258 (2012) 4063–4068.
- [24] M. Jin, Y. Shen, X. Luo, J. Tao, Y. Xie, H. Chen, Y. Wu, A combination structure of microblock and nanohair fabricated by chemical etching for excellent water repellency and icephobicity, *Appl. Surf. Sci.* 455 (2018) 883–890.
- [25] C.R. Crick, J.C. Bear, P. Southern, I.P. Parkin, A general method for the incorporation of nanoparticles into superhydrophobic films by aerosol assisted chemical vapour deposition, *J. Mater. Chem. A* 1 (2013) 4336–4344.
- [26] N. Zhang, S. Lu, W. Xu, Y. Zhang, Controlled growth of CuO–Cu<sub>3</sub>Pt/Cu micro-nano binary architectures on copper substrate and its superhydrophobic behavior, *New J. Chem.* 38 (2014) 4534–4540.
- [27] T. Darmanin, E.T. de Givenchy, S. Amigoni, F. Guittard, Superhydrophobic surfaces by electrochemical processes, *Adv. Mater.* 25 (2013) 1378–1394.
- [28] P. Tourkine, M. Le Merrer, D. Quere, Delayed freezing on water repellent materials, *Langmuir* 25 (2009) 7214–7216.
- [29] Z. Zuo, X. Song, R. Liao, X. Zhao, Y. Yuan, Understanding the anti-icing property of nanostructured superhydrophobic aluminum surface during glaze ice accretion, *Int. J. Heat Mass Tran.* 133 (2019) 119–128.
- [30] A. Davis, Y.H. Yeong, A. Steele, L.S. Bayer, E. Loth, Superhydrophobic nanocomposite surface topography and ice adhesion, *ACS Appl. Mater. Interf.* 6 (2014) 9272–9279.
- [31] G. Jiang, L. Chen, S. Zhang, H. Huang, Superhydrophobic SiC/CNTs coatings with photothermal deicing and passive anti-icing properties, *ACS Appl. Mater. Interf.* 10 (2018) 36505–36511.
- [32] Z. Zhao, H. Chen, X. Liu, H. Liu, D. Zhang, Development of high-efficient synthetic electric heating coating for anti-icing/de-icing, *Surf. Coat. Technol.* 349 (2018) 340–346.
- [33] Y. Liu, X. Li, J. Jin, J. Liu, Y. Yan, Z. Han, L. Ren, Anti-icing property of bio-inspired micro-structure superhydrophobic surfaces and heat transfer model, *Appl. Surf. Sci.* 400 (2017) 498–505.
- [34] O. Parent, A. Ilinca, Anti-icing and de-icing techniques for wind turbines: critical review, *Cold Reg. Sci. Technol.* 65 (2011) 88–96.
- [35] A. Cassie, S. Baxter, Wettability of porous surfaces, *Trans. Faraday Soc.* 40 (1944) 546–551.
- [36] V.V. Antic, M.N. Govedarical, J. Djonlagic, The effect of the mass ratio of hard and soft segments on some properties of thermoplastic poly(ester-siloxane)s, *Polym. Int.* 53 (2004) 1786–1794.
- [37] N.A. Patankar, On the modeling of hydrophobic contact angles on rough surfaces, *Langmuir* 19 (4) (2003) 1249–1253.
- [38] Y. Cheng, S. Lu, W. Xu, Controllable wettability of micro- and nano-dendritic structures formed on aluminum substrates, *New J. Chem.* 39 (2015) 6602–6610.
- [39] E. Moretti, M. Lenarda, L. Storaro, A. Talon, T. Montanari, G. Busca, E. Rodríguez-Castellón, A. Jiménez-López, M. Turco, G. Bagnasco, R. Frattini, One-step synthesis of a structurally organized mesoporous CuO-CeO<sub>2</sub>-Al<sub>2</sub>O<sub>3</sub> system for the preferential CO oxidation, *Appl. Catal. A-Gen.* 335 (2008) 46–55.
- [40] F.E. López-Suárez, A. Bueno-López, M.J. Illán-Gómez, Cu/Al<sub>2</sub>O<sub>3</sub> catalysts for soot oxidation: copper loading effect, *Appl. Catal. B-Environ.* 84 (2008) 651–658.
- [41] M.-D. Pei, B. Wang, E. Li, X.-H. Zhang, X.-M. Song, H. Yan, The fabrication of superhydrophobic copper films by a low-pressure-oxidation method, *Appl. Surf. Sci.* 256 (2010) 5824–5827.
- [42] H. Zhang, J.-L. Cao, G.-S. Shao, Z.-Y. Yuan, Synthesis of transition metal oxide nanoparticles with ultrahigh oxygen adsorption capacity and efficient catalytic oxidation performance, *J. Mater. Chem.* 19 (2009) 6097.
- [43] G. Wang, T.Y. Zhang, Oxygen adsorption induced superhydrophilic-to-superhydrophobic transition on hierarchical nanostructured CuO surface, *J. Colloid Interf. Sci.* 377 (2012) 438–441.
- [44] H. Gao, H. Yao, Shape insensitive optimal adhesion of nanoscale fibrillar structures, *Proc. Natl. Acad. Sci. USA* 101 (2004) 7851–7856.
- [45] A. Peigney, C. Laurent, E. Flahaut, R.R. Bacsá, A. Rousset, Specific surface area of carbon nanotubes and bundles of carbon nanotubes, *Carbon* 39 (2001) 507–514.
- [46] T. Maitra, S. Jung, M.E. Giger, V. Kandrial, T. Ruesch, D. Poulikakos, Superhydrophobicity vs. ice adhesion: the quandary of robust icephobic surface design, *Adv. Mater. Interf.* 2 (2015) 1500330.
- [47] A. Criscione, I.V. Roisman, S. Jakirlić, C. Tropea, Towards modelling of initial and final stages of supercooled water solidification, *Int. J. Therm. Sci.* 92 (2015) 150–161.
- [48] M. Schremb, S. Borchert, E. Berberovic, S. Jakirlić, I.V. Roisman, C. Tropea, Computational modelling of flow and conjugate heat transfer of a drop impacting onto a cold wall, *Int. J. Heat Mass Tran.* 109 (2017) 971–980.
- [49] P.M.M. Pereira, A.S. Moita, G.A. Monteiro, D.M.F. Prazeres, Characterization of the topography and wettability of English weed leaves and biomimetic replicas, *J. Bionic Eng.* 11 (2014) 346–359.
- [50] S.S. Latthe, P. Sudhagar, A. Devadoss, A.M. Kumar, S. Liu, C. Terashima, K. Nakata, A. Fujishima, A mechanically bendable superhydrophobic steel surface with self-cleaning and corrosion-resistant properties, *J. Mater. Chem. A* 3 (2015) 14263–14271.
- [51] C. Tan, Q. Li, P. Cai, N. Yang, Z. Xi, Fabrication of color-controllable superhydrophobic copper compound coating with decoration performance, *Appl. Surf. Sci.* 328 (2015) 623–631.